ACS OMEGA

http://pubs.acs.org/journal/acsodf

Article

Evidence of a Thermal Diffusivity Gap in Sintered Li−Co−Sb−O Solid Solutions

Nelson W. Pech-May,* Carolina Tabasco-Novelo,* Patricia Quintana,* Geonel Rodriguez-Gattorno,* and Juan J. Alvarado-Gil*

Cite This: *ACS Omega* 2023, 8, 7808−7815

Read Online

ACCESS | Metrics & More | Article Recommendations | Supporting Information

ABSTRACT: In this work, the thermal properties of ternary $Li_{3x}Co_{7-4x}Sb_{2+x}O_{12}$ solid solutions are studied for different concentrations in the range $0 \leq x \leq 0.7$. Samples are elaborated at four different sintering temperatures: 1100, 1150, 1200 and 1250 °C. The effect of increasing the content of Li^+ and Sb^{5+}, accompanied by the reduction of Co^{2+}, on the thermal properties is studied. It is shown that a thermal diffusivity gap, which is more pronounced for low values of *x*, can be triggered at a certain threshold sintering temperature (around 1150 °C in this study). This effect is explained by the increase of contact area between adjacent grains. Nevertheless, this effect is found to be less pronounced in the thermal conductivity. Moreover, a new framework for heat diffusion in solids is presented that establishes that both the heat flux and the thermal energy (or heat) satisfy a diffusion equation and therefore highlights the importance of thermal diffusivity in transient heat conduction phenomena.

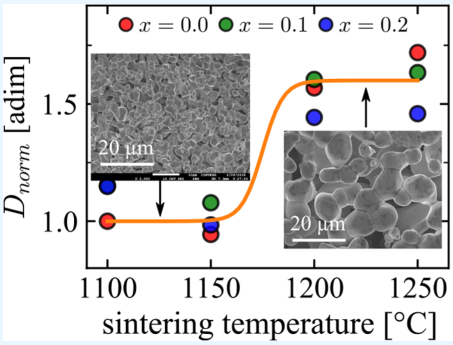

Li-Co-Sb-O solid solutions:
$Li_{3x}Co_{7-4x}Sb_{2+x}O_{12}$
$0.0 \leq x \leq 0.7$

■ INTRODUCTION

Ceramic oxides with spinel structures are a class of versatile materials that possess outstanding physical properties that make them useful in the design and operation of a wide variety of technological applications. For example, these materials have been used as diluted magnetic semiconductors (DMS),[1−3] catalysts,[4,5] thermistors,[6] and pigments,[7] among others.[8,9] Spinel compounds with pentavalent ($Zn_7Sb_2O_{12}$) and divalent ($Co_7Sb_2O_{12}$) cations have shown high potential as ceramic varistors.[10] In particular, the binary spinel $Co_7Sb_2O_{12}$ has attracted interest, since the ion distribution of Co^{2+} in the tetrahedral and octahedral sites into the spinel structure can be affected by the high valence of the Sb^{5+} ion and high sintering temperatures.[1,11] Physical properties of spinel oxides depend on the cation distribution through the tetrahedral and octahedral sites in the structure, as Co^{2+} ions occupy both sites but have a preference for octahedral sites and Sb^{5+} is restricted to octahedral sites;[10] when Li is added to $Co_7Sb_2O_{12}$, a new solid solution is obtained and the cation distribution changes, consequently modifying the physical properties. Accordingly, it was recently shown that $Li_{3x}Co_{7-4x}Sb_{2+x}O_{12}$ solid solutions exhibit nonohmic properties with a high electric field threshold like those common ceramic varistors as of ZnO and SnO_2.[12] Furthermore, binary and ternary solid solution ceramics have been proposed and successfully applied in thermoelectrics and as electrodes for lithium-ion batteries.[13,14] In these applications, heat transport is one of the most important factors to keep in mind for the design and during the operation of such devices. Accordingly, a thorough study of the thermal properties of the new solid solutions is required to determine if they can be used in one or another future applications.

In this work, $Li_{3x}Co_{7-4x}Sb_{2+x}O_{12}$ solid solutions in the range $0 \leq x \leq 0.7$ are fabricated at four different sintering temperatures: 1100, 1150, 1200, and 1250 °C, where the sintering pressure is kept constant. The thermal diffusivity and thermal conductivity are analyzed in the heat diffusion regime as functions of *x* and the sintering temperature. It is shown, for the first time, that a thermal diffusivity gap, which is more pronounced for low values of *x*, can be triggered at a certain threshold sintering temperature, around 1150 °C for these Li−Co−Sb−O solid solutions. Briefly, below the threshold sintering temperature, the thermal diffusivity increases monotonically with *x*, but for sintering temperatures above 1150 °C the thermal diffusivity shows a large increase for $x \leq 0.4$ with respect to the values at lower sintering temperatures, and for $x > 0.4$ the thermal diffusivity increases almost in the same way for all the sintering temperatures tested. This effect is explained in terms of the roles

Received: November 25, 2022
Accepted: February 8, 2023
Published: February 16, 2023

https://doi.org/10.1021/acsomega.2c07557
ACS Omega 2023, 8, 7808−7815

of the thermal diffusivity and thermal conductivity in heat conduction phenomena.

Our work paves the way to further research, selection and application of novel ceramic varistors based on the thermophysical properties. Moreover, we spotlight the diffusion behavior of the heat flux and the thermal energy, complementary to that of the temperature field. This directly suggests a novel way for the theoretical modeling of heat diffusion in solids, as well as for the study of thermal properties of solids, by directly monitoring the power or energy evolution rather than the temperature.

■ MATERIALS AND METHODS

Synthesis of Li−Co−Sb−O Solid Solutions. The samples were synthesized according to the formula $Li_{3x}Co_{7-4x}Sb_{2+x}O_{12}$ in the range $0 \le x \le 0.7$. The reagents CoO (99.995%, Sigma-Aldrich), Li_2CO_3 (+99%, Sigma-Aldrich), and Sb_2O_5 (99.99%, Sigma-Aldrich) were preheated at 115 °C to remove the water content. The starting materials were weighted out in stoichiometric amounts to give 5 g total. Subsequently, they were mixed in an agate mortar and pestle with acetone and dried and heated in alumina crucibles. Initially, the temperature was increased slowly from room temperature (25 °C) up to 750 °C at a rate of 2 °C/min, and this temperature was maintained for 6 h to drive off the water content and eliminate CO_2. The samples inside the furnace were cooled until the room temperature (25 °C) was reached and then were removed from the furnace for further characterization. Immediately, they were grounded with acetone prior to a second annealing from 800 to 1000 °C with a step rise of 50 °C every 24 h. After heating at 1000 °C, the powder samples were pressed at 11.5 MPa for 2 min into pellets of around 7 mm diameter. Table 1 shows the measured dimensions (thickness and diameter) of all 32 test samples. These samples were sintered at four different sintering temperatures, 1100, 1150, 1200 and 1250 °C, for 24 h with heating/cooling rates of 3 °C/min. The pellet density was determined from its weight and final dimensions.

Table 1. Measured Dimensions of $Li_{3x}Co_{7-4x}Sb_{2+x}O_{12}$ Test Samples

x value	1100 °C	1150 °C	1200 °C	1250 °C
thickness (mm)				
0.0	0.896	1.230	1.220	0.878
0.1	0.957	1.464	1.007	0.866
0.2	0.578	1.331	0.930	0.852
0.3	0.579	0.621	1.329	0.913
0.4	0.558	0.631	0.943	1.012
0.5	0.513	1.224	0.863	1.301
0.6	0.610	0.901	0.912	1.310
0.7	0.893	0.747	0.909	1.402
diameter (mm)				
0.0	7.195	7.162	6.935	7.228
0.1	7.115	7.115	6.927	6.916
0.2	7.073	7.157	6.908	6.974
0.3	7.105	7.007	7.123	7.014
0.4	7.075	7.007	6.947	7.028
0.5	7.075	7.047	6.933	6.987
0.6	6.980	6.965	6.915	6.949
0.7	7.035	6.988	6.950	6.932

Structural Characterization Methods. Crystalline phase analysis and the determination of the crystallinity of the solid solutions were performed using X-ray diffraction (XRD) with a D8 Advance Bruker diffractometer with monochromatic Cu Kα radiation. Diffraction patterns were measured from $10° \le 2\theta \le 60°$ at 0.04°/s.

The average grain size of the sample was determined from the analysis of the scanning electron microscopy (SEM) images. A Jeol Microscope model JSM-7600F was used to take the SEM images. The pellets were etched in $HClO_4$ diluted in water in a ratio of 1:1000 to reveal their morphological characteristics. SEM images were taken using a SEI (secondary electron imaging) detector in order to observe topographic features.

Sample Density. The bulk density ρ of each sample, in kg/m^3, was computed based on the basic principle of dividing its measured mass (m) by its volume (V). That is, by definition $\rho = m/V$. Therefore, the mass of each sample was measured using an analytical balance, and the volume was obtained from the measured diameter and thickness of the disc samples. Both the sample thickness and diameter (see Table 1) and the sample weight were tested repeatedly (at least five times). The density was determined using the given definition, and the uncertainty in the estimated value was additionally evaluated using error propagation.[15]

Modulated Differential Scanning Calorimetry (m-DSC). The heat capacity of the pellets was analyzed by means of modulated differential scanning calorimetry, which measures the difference in the heat flux between a sample and an inert reference as a function of time and temperature. A sinusoidal heat modulation is applied over a linear heating/cooling ramp to obtain a profile in which the average temperature of the sample changes continuously with time in a nonlinear way. The sinusoidal heating rate provides the heat capacity information. A modulated differential scanning calorimeter (TA Instruments Discovery DSC) was used for all measurements. A heating rate of 2 °C/min in a sealed aluminum pan under dynamic N_2 atmosphere was set for all samples, and sapphire was used as the reference material. Modulation temperature ±1 °C with a period of 100 s was used for the modulated component.

Front-Face Flash Method (F3M). The thermal diffusivity of the solid solutions was studied using the front-face flash method. It has been shown that this method allows fast and accurate measurements of the heat transport properties in solids.[16−18] Moreover, it is specially suited for opaque and black solid samples, as is the case of the Li−Co−Sb−O solid solutions studied in this work. Briefly, the surface of the sample (solid slab) is uniformly heated using a short light pulse. Subsequently, the temperature evolution of the surface (heating and cooling) is recorded using an infrared (IR) detector or IR camera. An analytical solution for the surface temperature of the solid slab is available in the Laplace domain,[19]

$$\overline{T}(z=0,\,s) = \frac{\overline{I}_0\chi}{\epsilon}\,\frac{\sqrt{s} + h'\tanh(y\sqrt{s})}{2h'\sqrt{s} + (s + h'^2)\tanh(y\sqrt{s})} \qquad (1)$$

where $\overline{T}(z=0,\,s)$ is the Laplace transform of the surface temperature, s is the Laplace variable, χ is the energy fraction absorbed by the front surface, and ϵ is the thermal effusivity of the solid. $h' = h/\epsilon$, where h is the convective heat loss coefficient from both surfaces to the surroundings. $y = L/\sqrt{D}$, where L is the thickness of the slab and D its thermal diffusivity. $\overline{I}_0 = Q_0(1 - e^{-\tau s})/s$ represents the Laplace transform of a light pulse with a step-like temporal shape and duration τ. Q_0 is the power per unit area delivered by the light pulse.

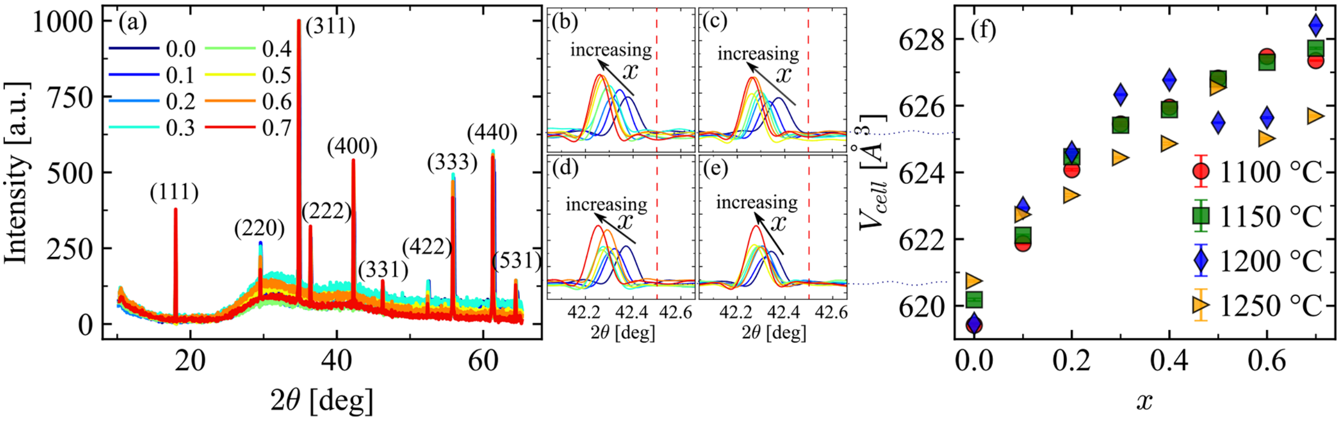

Figure 1. (a) Diffractograms of $Li_{3x}Co_{7-4x}Sb_{2+x}O_{12}$ solid solutions for $0 \leq x \leq 0.7$. Zoomed-in views around the (400) reflection for (b) 1100, (c) 1150, (d) 1200, and (e) 1250 °C sintering temperatures. (f) Unit cell volume as a function of the x value for the four different sintering temperatures.

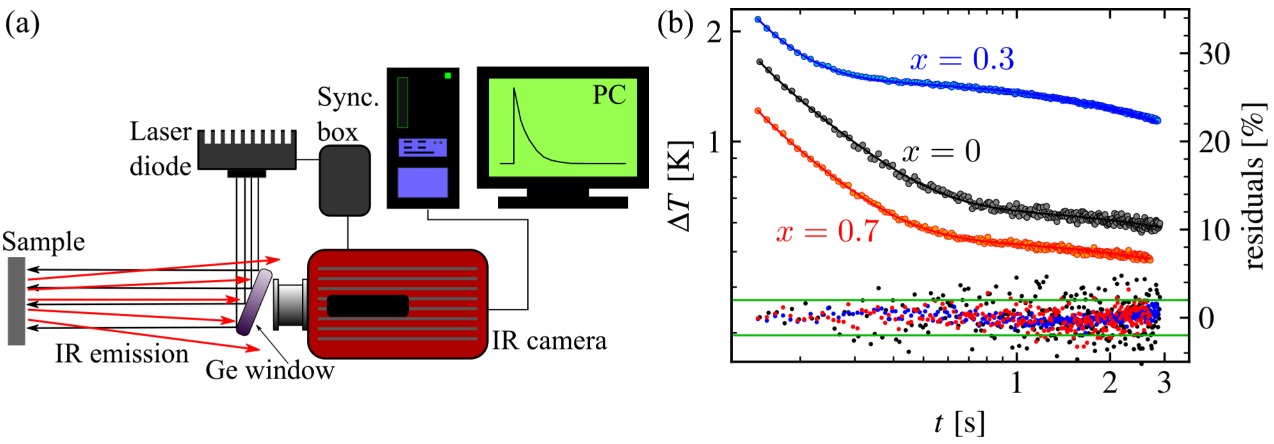

Figure 2. (a) Diagram of the F3M setup used for measuring the thermal diffusivity of $Li_{3x}Co_{7-4x}Sb_{2+x}O_{12}$ solid solutions. (b) Typical surface temperature evolution plots for three different x values in the solid solutions. Dots are experimental data, and continuous lines correspond to the fittings to the model presented in subsection F3M (see eq 1).

The surface temperature evolution $T(z = 0, t)$ is obtained from eq 1 by an inverse Laplace transform. This is done numerically using the well-known Euler algorithm[20] for both the heating and cooling stages. Further details about the implementation can be found in previous investigations.[18,21] The surface temperature evolution can be expressed as $T(p_1, p_2, p_3; z = 0, t)$, where $p_1 = Q_0\chi/\epsilon$, $p_2 = L/\sqrt{D}$, and $p_3 = h'$. Consequently, it involves three unknown parameters that can be obtained by fitting the inverse Laplace transform of eq 1 to the measured surface temperature evolution. In particular, we are interested in parameter $p_2 = L/\sqrt{D}$, from which the thermal diffusivity is obtained if the thickness of the slab is previously known.

Figure 2a shows a diagram of the experimental setup based on the front-face flash method (F3M) used to measure the thermal diffusivity of the Li−Co−Sb−O solid solutions. A laser diode (976 nm wavelength) operated with 800 mW power is used as the excitation source. A step-like illumination is triggered via the synchronization box of the IR camera. The step duration is 100 ms for these measurements. A cooled IR camera (InfraTec 8320 working in the 3−5 μm spectral range) is used to record the IR emission from the sample surface. Each pixel in the detector averages the IR emission coming from a square of 0.135×0.135 mm^2. The thermograms (IR images) are recorded at 500 frames per second. The samples have good absorption at the laser wavelength and good emission in the operating IR range of the camera detectors. Consequently, they are measured without further preparation (see Figure S4 in the Supporting Information). However, the IR camera only collects data proportional to the temperature increase (ΔT) of the sample with respect to the room temperature. The actual value of the temperature rise is not previously known because the exact emissivity of the samples is also unknown. Figure 2b shows typical surface temperature evolution curves obtained for $Co_7Sb_2O_{12}$ (in black, x = 0), $Li_{0.9}Co_{5.8}Sb_{2.3}O_{12}$ (in blue, x = 0.3), and $Li_{2.1}Co_{4.2}Sb_{2.7}O_{12}$ (in red, x = 0.7). Dots are the experimental data collected, and continuous lines are the curve fittings to the model presented in the F3M subsection. For the sake of clarity, only one point out of ten is displayed. However, all data points are included in the fits. The numerical inverse Laplace transform of eq 1 is fitted to the experimental results using a least-squares fitting procedure based on the well-known Levenberg−Marquardt algorithm. Only three parameters are used in the fits: p_1, p_2, and p_3. From $p_2 = L/\sqrt{D}$, the thermal diffusivity is retrieved using the measured thickness of the sample. The residuals, i.e., the normalized difference between experimental data and fitted values, $100 \times (T_{exp} - T_{fit})/T_{exp}$, are also shown. The two horizontal green lines in Figure 2b indicate the ±2% residuals, showing the accuracy of the fits.

Finally, we would like to point out that the *thermal diffusivity* gives a measure of the area over which heat spreads per unit of time (easier to picture while temperature is evolving, i.e., during a transient). In contrast, the *thermal conductivity* measures the power per unit area that is required to establish a temperature gradient (easier to picture when the temperature gradient does not change over time, i.e., when the steady-state is reached).

■ RESULTS AND DISCUSSION

Structural Characterization. Figure 1a shows the X-ray diffractograms of $Li_{3x}Co_{7-4x}Sb_{2+x}O_{12}$ pellets in the range $0.0 \leq x \leq 0.7$, which corresponds to the spinel phase $Co_7Sb_2O_{12}$. The powder diffractograms show that the reflection (400) at 42.29° shifts to lower values of 2θ with increasing values of x in $Li_{3x}Co_{7-4x}Sb_{2+x}O_{12}$.[12] The red vertical dashed line at 42.5°(2θ) belongs to the (400) reflection of the cobalt spinel reported on the ICDD standards (PDF 00-015-0517). The shift effect at different sintering temperatures is shown in Figure 1b−e for 1100, 1150, 1200, and 1250 °C, respectively. It was found that at low temperatures the shift has a small effect, however, it increases at 1200 and 1250 °C. Therefore, the intensity decreases when the sintering temperature increases and the reflections are slightly shifted to higher 2θ values, in contrast to the regular trend.

Using Rietveld refinement, the lattice parameter for each composition was calculated and the unit cell volume (V_{cell}) was plotted as a function of the x value in Figure 1f. It can be observed that the cell volume grows as the content of Li^+ and Sb^{5+} increases, i.e., higher x values in the samples. This trend can be explained considering the crystal radius of Co^{2+} ($r^{IV} = 0.72$ Å and $r^{VI} = 0.885$ Å high spin and 0.79 Å low spin), Li^+ ($r^{IV} = 0.73$ Å and $r^{VI} = 0.90$ Å), and Sb^{5+} ($r^{VI} = 0.74$ Å), as well as the site occupancy preference of Co^{2+} for tetrahedral sites and that Sb^{5+} is constrained to occupy only octahedral sites.[3,22,23] In both octahedral and tetrahedral sites, the Li^+ radius is larger than the Co^{2+} radius; therefore, when the cobalt concentration decreases, the unit cell increases suddenly, indicating that Li^+ is replacing Co^{2+} in the octahedral sites. Additionally, Figure 1f shows a deviation from linearity for $x > 0.3$ and the growth in the unit cell volume is smaller, indicating that for higher compositions the Li^+ also occupies the tetrahedral sites. Additionally, the expected trend for each composition is the growth of the unit cell volume with the increase of the sintering temperature. However, the decrease observed in the unit cell volume for the highest sintering temperature is related to the evaporation of Li.[24] Harrington et al.[23] pointed out that the cation disorder in some way is specific in a sample and dependent on the synthesis condition and temperature, and the degree of cation disorder is observed by means of a variation in the lattice parameter.

Figure 3a−d show scanning electron microscopy images of $Li_{0.9}Co_{5.8}Sb_{2.3}O_{12}$ ($x = 0.3$) corresponding to sintering temperatures from 1100 to 1250 °C. These SEM images show that the pore size and the grain size increase during coarsening at high temperatures. Additionally, it is shown that the contact area between the grains improves as the sintering temperature rises. This later effect can induce an improvement on the heat transport of the Li−Co−Sb−O solid solutions.[25] Furthermore, a collection of SEM images at each x and each sintering temperature is presented in Figure S2 of the Supporting Information. Figure 3e shows the grain size at each sintering temperature as a function of x in $Li_{3x}Co_{7-4x}Sb_{2+x}O_{12}$. Here, it is confirmed at each x that the average grain size increases with the sintering temperature, in accordance with the Arrhenius law.[26]

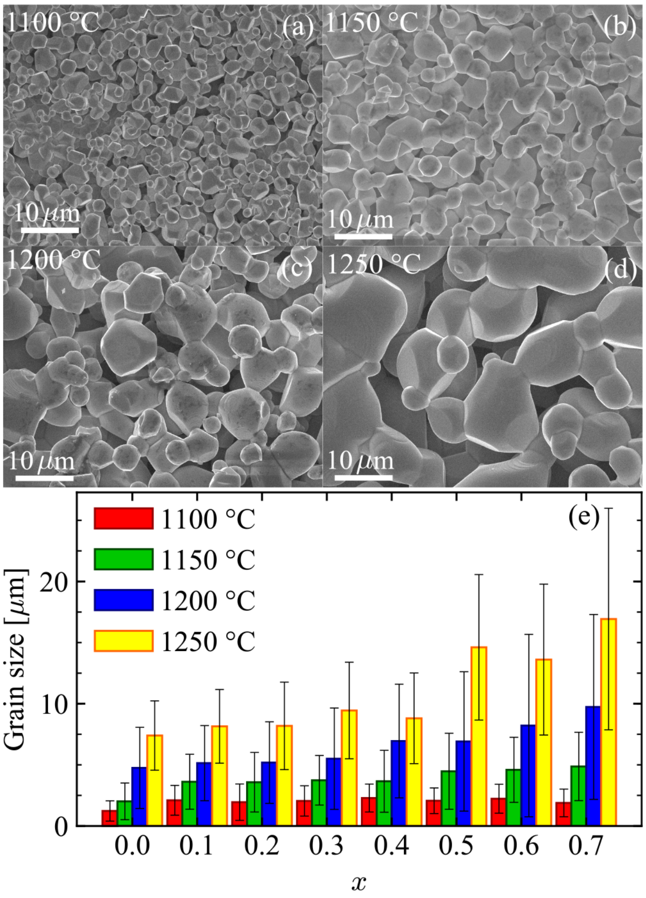

Figure 3. SEM images of $x = 0.3$ at (a) 1100, (b) 1150, (c) 1200, and (d) 1250 °C. (e) Grain size results for the solid solutions at the studied sintering temperatures.

Moreover, the grain size increases as a function of x at each sintering temperature. For example, it increases from 7.4 ± 2.8 to 17 ± 9.1 μm at 1250 °C. The error bars represent the variation of the grain size. This suggests that increasing the Li/Sb content favors the coarsening processes.

Thermal Characterization. We first present and discuss the results obtained for the bulk density ρ of the samples. Four different sintering temperatures are analyzed here: 1100, 1150, 1200, and 1250 °C. The obtained results are presented in Figure 4a as a function of x. The color code used is shown in Figure 4c, and the error bars are obtained from the standard error of five measurements.[15] No clear dependence as a function of x is obtained for 1100 and 1150 °C. In contrast, for the two highest sintering temperatures, ρ depends definitely on x. Minimum density values are obtained in the range $0.2 \leq x \leq 0.4$ and at $x = 0.3$ for 1200 and 1250 °C sintering temperatures, respectively. This tendency is in accordance with the increase of the pore size previously illustrated in the SEM analysis. That is, even when the contact area between grains is larger for these sintering temperatures, the porosity of the sample increases. We think that this is because of coarsening and the fact that the compression stress is constant during the sintering process but the mechanical properties of the grains (bulk modulus and Poisson's ratio) depend on the temperature, therefore affecting the final deformation of the grains. Because of the increase of porosity (reduction in density) at some x values, a corresponding reduction of the thermal conductivity is expected.[27] The density as a function of the sintering

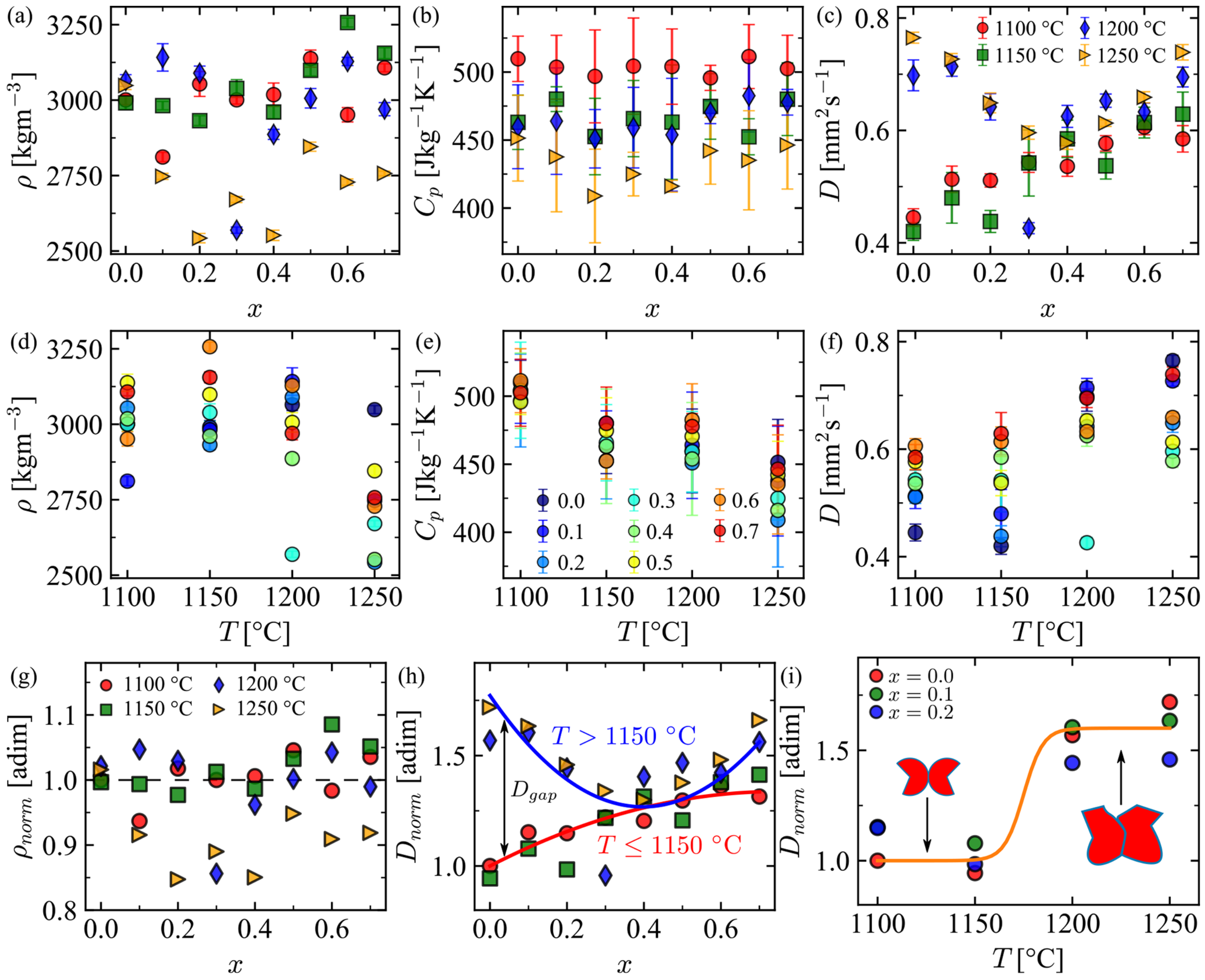

Figure 4. (a) Density, (b) specific heat capacity at constant pressure, and (c) thermal diffusivity as a function of x in $Li_{3x}Co_{7-4x}Sb_{2+x}O_{12}$ solid solutions. The influence of the different sintering temperatures is shown in each case. (d) Density, (e) specific heat capacity at constant pressure, and (e) thermal diffusivity as a function of the sintering temperature T. The effect of the concentration at each sintering temperature is shown. (g) Normalized density as a function of x. The two lowest sintering temperatures are almost constant, and the two largest show some dependence with x (and are affected by the porosity). (h) Normalized thermal diffusivity as a function of x. A thermal diffusivity gap (or discontinuity) is found around the 1150 °C sintering temperature. (i) Normalized thermal diffusivity as a function of the sintering temperature for low values of x. The diagrams elucidate the reason for the thermal diffusivity gap obtained. Dashed and continuous lines mark the tendency.

temperature (T) is shown in Figure 4d. It is clear that only at 1250 °C does the density decrease for the majority of x values. This indicates that at this sintering temperature the porosity is higher for almost all x values, in contrast with the results at lower sintering temperatures. Additionally, considering that this decrease in ρ is only due to increase in porosity, then a corresponding decrease in heat capacity is expected.

Figure 4b shows the specific heat capacity at constant pressure (C_p) obtained using m-DSC. The same markers and colors as in Figure 4a and c are used. The error bars are obtained as mentioned above. Note that C_p is practically independent of the Li^+ and Sb^{5+} content. However, the specific heat capacity tends to decrease as the sintering temperature increases. This is better represented in Figure 4e as a function of the sintering temperature. Here, the reduction in the ability to store thermal energy can be attributed to coarsening, which increases the porosity despite the fact that the grain size increases with T. Nevertheless, for 1150 and 1200 °C sintering temperatures, the specific heat capacity is almost equal, independent of the x value.

The thermal diffusivity as a function of x and T is presented in Figure 4c and f, respectively. For the two lowest sintering temperatures (1100 and 1150 °C), the thermal diffusivity increases progressively with x, but this is no longer the case for 1200 and 1250 °C. Rather, for these sintering temperatures, the thermal diffusivity decreases monotonically for low values of x ($0 \leq x \leq 0.4$) and increases progressively for $x > 0.4$, just as in the case of the two lowest sintering temperatures. Accordingly, in the representation as a function of T, two levels of thermal diffusivity can be distinguished for $x \leq 0.4$: a low level ∼0.5 mm^2/s for $T \leq 1150$ °C and a high level ∼0.75 mm^2/s for $T > 1150$ °C. In contrast, for $x > 0.4$, the thermal diffusivity only increases progressively as a function of T. To gain more insight of this effect on the thermal diffusivity, lets take a closer look at the normalized density (ρ_{norm}) and the normalized thermal diffusivity (D_{norm}). Both properties are normalized with respect to their values at $x = 0$ and $T = 1100$ °C. Figure 4g shows that the normalized density varies around $\rho_{\mathrm{norm}} = 1$ for 1100 and 1150 °C sintering temperatures, and the effect of porosity (as showed in the SEM analysis) appears for $T > 1150$ °C. In particular, for $T = 1250$ °C, the normalized density reduces around 10% in average. Therefore, similar trends should be observed in D_{norm} due to porosity effects. Figure 4h shows that besides the porosity effects, there is a clear difference between the thermal diffusivity values obtained for sintering temperatures $T \leq 1150$ °C and those for $T > 1150$ °C when $x \leq 0.4$. Based on the SEM images and the thermal diffusivity behavior, we suggest that this effect is also related to changes in the mechanical properties of the grains around 1150 °C (they become softer) such that below this sintering temperature the grains are more spherical and rigid and therefore the contact surface between them is not that large, but above this temperature the grains grow and the contact surface between them also increases because they become softer. This concept is shown in the diagrams in Figure 4i and can be confirmed by looking at the SEM images presented in Figure S2 of the Supporting Information. Since this effect is more pronounced for low x values, Figure 4i shows the normalized thermal diffusivity in the range $0 \leq x \leq 0.2$ as a function of the sintering temperature. Two levels of thermal diffusivity can be distinguished, which can be explained as follows: for sintering temperatures below a threshold $T_{\mathrm{th}} = 1150$ °C, the contact surface between grains is small and heat diffuses at a slow rate, which triggers the *low* thermal diffusivity level. However, above this threshold temperature, the crystallite size tends to increase, allowing a reduced scattering of heat carriers inside individual grains; at the same time, larger crystallites favor the increase of the contact between neighboring crystals, which also enhances heat transfer rate, triggering the *high* thermal diffusivity level in the Li−Co−Sb−O solid solutions. Accordingly, a *thermal diffusivity gap* (D_{gap}) is exceeded above the sintering temperature threshold ($T_{\mathrm{th}} = 1150$ °C). This behavior resembles the operation principle of a typical laser diode, where a threshold current should be exceeded to properly operate the laser. Nevertheless, increasing the operating current increases proportionally the laser output power, which is apparently not the case here. Therefore, a wider range of sintering temperatures should be tested to make a better comparison.

Thermal Conductivity. The effective thermal conductivity of the Li−Co−Sb−O solid solutions is determined by means of the well-known relation,[27] $K = D\rho C_p$, using the material properties obtained in the previous subsection. Error propagation is used for estimation of the standard errors in K.[15] Figure 5a and b show the thermal conductivity as a function of x and T, respectively.

Even though a similar trend to the thermal diffusivity as a function of x is observed here, it is clear that the thermal conductivity gap is smaller. That is, the effect is masked by the density and heat capacity of the solid solutions. This can be better explained by the physical meaning of thermal diffusivity and thermal conductivity, as explained at the end of section Front-Face Flash Method (F3M). Accordingly, increasing the contact area between the grains will have a larger impact in the effective thermal diffusivity of the grain−grain system, while it will only induce an indirect change in the effective thermal conductivity.

The maximum thermal conductivity obtained is ∼1 W/m·K, and the minimum is around 0.5 W/m·K. The upper limit is fixed by the microstructure of the solid solutions. It is well-known that the presence of voids in sintered and granular media reduces drastically the thermal performance. Additionally, a reduction in thermal conductivity for intermediate values of x has been previously shown to be induced by the scattering of low-frequency phonons by point defects in disordered semiconductor alloys.[28,29] On the other hand, the lower limit of the thermal conductivity can be partially attributed to the changes in the lattice parameter, as inferred from the XRD diffractograms in Figure 1, because it contributes actively to the scattering of low-frequency phonons by point defects.

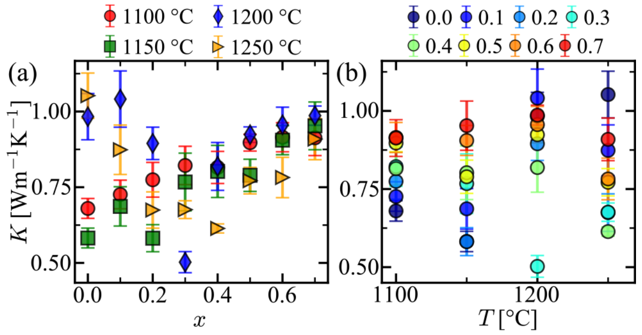

Figure 5. (a) Thermal conductivity as a function of x in $Li_{3x}Co_{7-4x}Sb_{2+x}O_{12}$. (b) Thermal conductivity as a function of the sintering temperature T.

A Framework for Heat Diffusion in Solids. As final remark, we would like to introduce a new framework for heat diffusion in solids, which can be also very useful in the analysis of heat conduction in sintered and granular materials. According to Fourier's law, the rate of heat conduction per unit area (or heat flux $q = \partial h/\partial t$ in W/m^2) is proportional to the temperature gradient $q = K\partial T/\partial x$, where K is the thermal conductivity in W/m·K and T is the temperature. On that premise, here we show that the rate of heat flux is proportional to its Laplacian ($\partial^2 q/\partial x^2$). That is

$$\frac{\partial}{\partial t}\underbrace{\left(-K\frac{\partial T}{\partial x}\right)}_{q} = D\frac{\partial^2}{\partial x^2}\underbrace{\left(-K\frac{\partial T}{\partial x}\right)}_{q} \tag{2}$$

where the commutation properties $[\partial/\partial t, -K\partial/\partial x] = 0$ and $[\partial^2/\partial x^2, -K\partial/\partial x] = 0$ were applied to the well-known heat diffusion equation ($\partial T/\partial t = D\partial^2 T/\partial x^2$). Therefore

$$\frac{\partial q}{\partial t} = D\frac{\partial^2 q}{\partial x^2} \tag{3}$$

$$\frac{\partial h}{\partial t} = D\frac{\partial^2 h}{\partial x^2} \tag{4}$$

where D is the thermal diffusivity in m^2/s, h is the heat per unit area (or thermal energy per unit area in J/m^2) and q is the rate of heat conduction per unit area (or heat flux) in W/m^2. Note that eqs 3 and 4 are analogous to the heat diffusion equation, but instead of relating the temperature here we have obtained a diffusion equation for the heat flux itself (see eq 3) and similarly for the thermal energy per unit area (see eq 4). In summary, heat diffusion in solids can be studied by monitoring either the temperature, the heat flux, or the thermal energy.

■ CONCLUSIONS

In this work, the thermal properties of $Li_{3x}Co_{7-4x}Sb_{2+x}O_{12}$ solid solutions were studied. The concentration was varied in the range $0 \leq x \leq 0.7$, and four different sintering temperatures

(1100, 1150, 1200 and 1250 °C) were considered. It was shown for the first time that a thermal diffusivity gap, which is more pronounced for low values of x, can be triggered at a certain threshold sintering temperature (~1150 °C in this case). This effect was explained by the increase of the contact area between adjacent grains. However, a lower impact was found in the thermal conductivity. This contrast was explained by the roles of thermal diffusivity and thermal conductivity in transient and steady-state heat conduction, respectively. Finally, we have shown that besides the temperature, the heat flux and thermal energy also satisfy diffusion equations, with the thermal diffusivity as the main parameter.

■ ASSOCIATED CONTENT

Supporting Information

The Supporting Information is available free of charge at https://pubs.acs.org/doi/10.1021/acsomega.2c07557.

> XRD diffractograms for each sintering temperature, SEM micrographs for $0 \leq x \leq 0.7$ at each sintering temperature, a description of the Li−Co−Sb−O sample elaboration, and the temperature dependence of V_{cell} (PDF)

■ AUTHOR INFORMATION

Corresponding Authors

Nelson W. Pech-May − *Applied Physics Department, CINVESTAV-Unidad Mérida, 97310 Mérida, Yucatán, Mexico; Bundesanstalt für Materialforschung und -prüfung (BAM), 12200 Berlin, Germany;* orcid.org/0000-0002-5822-482X; Email: nelson.pechmay@gmail.com

Carolina Tabasco-Novelo − *Applied Physics Department, CINVESTAV-Unidad Mérida, 97310 Mérida, Yucatán, Mexico*; Email: carolinatabasco@gmail.com

Patricia Quintana − *Applied Physics Department, CINVESTAV-Unidad Mérida, 97310 Mérida, Yucatán, Mexico*; Email: pquint@cinvestav.mx

Geonel Rodriguez-Gattorno − *Applied Physics Department, CINVESTAV-Unidad Mérida, 97310 Mérida, Yucatán, Mexico;* orcid.org/0000-0001-7438-6311; Email: geonelr@cinvestav.mx

Juan J. Alvarado-Gil − *Applied Physics Department, CINVESTAV-Unidad Mérida, 97310 Mérida, Yucatán, Mexico*; Email: juan.alvarado@cinvestav.mx

Complete contact information is available at: https://pubs.acs.org/10.1021/acsomega.2c07557

Notes

The authors declare no competing financial interest.

■ ACKNOWLEDGMENTS

This work was partially supported by Projects SEP-CONACYT-CB 256497, 182982, 178947, and 251882 "Investigación Científica Básica 2015"; Project 192 "Fronteras de la ciencia"; as well as the Fund Conacyt-SENER-Energy-Sustainability Grant 207450, within Strategic Project CEMIESol-Cosolpi no. 10 "Solar Fuel & Industrial Processes". Additionally, we acknowledge LANNBIO Cinvestav Mérida, under support from projects FOMIX-Yucatán 108160 CONACYT 123913, 188345, 204822, 292692, 294643, 294643, 299083, and 315860. N.W.P.-M. acknowledges his Adolf Martens postdoctoral fellowship 2019-2020. C.T.-N. acknowledges CONACYT for her Ph.D. scholarship. Technical help is acknowledged to M. Sc. D. Aguilar, M. Sc. Dora Huerta, and M. Sc. J. Bante-Guerra.

■ REFERENCES

(1) Ilic, A.; Antic, B.; Poleti, D.; Rodic, D.; Petrovic-Prelevic, I.; Karanovic, L. Cation distribution and magnetic properties of ternary spinels. *J. Phys.: Condens. Matter* **1996**, *8*, 2317−2325.

(2) Antic, B.; Rodic, D.; Tellgren, R.; Rundlof, H. Neutron diffraction study of the magnetic and structure properties of $Co_{2.50}Sb_{0.50}O_4$ spinel. *J. Magn. Magn. Mater.* **2000**, *219*, 41−44.

(3) Lisboa-Filho, P. N.; Vila, C.; Petrucelli, G.; Paiva-Santos, C. O.; Gama, L.; Ortiz, W. A.; Longo, E. Magnetic doping in $Zn_{7-x}M_xSb_2O_{12}$ spinels (M = Ni and Co). *Physica B* **2002**, *320*, 249−252.

(4) Zhang, L.; Yang, C.; Xie, Z.; Wang, X. Cobalt manganese spinel as an effective cocatalyst for photocatalytic water oxidation. *Appl. Catal., B* **2018**, *224*, 886−894.

(5) Osaki, T. Synthesis of $Zn_xCo_{3-x}O_4$ spinels at low temperature and atmospheric pressure. *J. Mater. Sci.* **2018**, *53*, 3250−3266.

(6) Nobre, M. A. d. L.; Lanfredi, S. Electrical characterization by impedance spectroscopy of $Zn_7Sb_2O_{12}$ ceramic. *Mater. Res.* **2003**, *6*, 151−156.

(7) Gouveia, D. S.; Soledade, L. E. B.; Paskocimas, C. A.; Longo, E.; Souza, A. G.; Santos, I. M. G. Color and structural analysis of $Co_xZn_{7-x}Sb_2O_{12}$ pigments. *Mater. Res. Bull.* **2006**, *41*, 2049−2056.

(8) Branković, Z.; Branković, G.; Poleti, D.; Varela, J. A. Structural and electrical properties of ZnO varistors containing different spinel phases. *Ceram. Int.* **2001**, *27*, 115−122.

(9) Ezhilvalavan, S.; Kutty, T. R. N. Low-voltage varistors based on zinc antimony spinel $Zn_7Sb_2O_{12}$. *Appl. Phys. Lett.* **1996**, *68*, 2693−2695.

(10) Brito, M. S. L.; Escote, M. T.; Santos, C. O. P.; Lisboa-Filho, P. N.; Leite, E. R.; Oliveira, J. B. L.; Gama, L.; Longo, E. Low-temperature synthesis of single-phase $Co_7Sb_2O_{12}$. *Mater. Chem. Phys.* **2004**, *88*, 404−409.

(11) Kawai, H.; Tabuchi, M.; Nagata, M.; Tukamoto, H.; West, A. Crystal chemistry and physical properties of complex lithium spinels $Li_2MM'_3O_8$ (M = Mg, Co, Ni, Zn; M'=Ti, Ge). *J. Mater. Chem.* **1998**, *8*, 1273−1280.

(12) Tabasco-Novelo, C.; Cervantes-López, J. L.; González-Panzo, I. J.; Rodríguez-Gattorno, G.; Quintana, P. High Non-Linear Electrical Properties of $Li_{3x}Co_{7-4x}Sb_{2+x}O_{12}$ a New Ceramic Varistor. *J. Alloys Compd.* **2021**, *878*, 160356.

(13) Wang, H.; Schechtel, E.; Pei, Y.; Snyder, G. J. High Thermoelectric Efficiency of N-type PbS - Wang - 2013 - Advanced Energy Materials - Wiley Online Library. *Adv. Energy Mater.* **2013**, *3*, 488−495.

(14) Hu, Y.; Li, Q.; Si, W. Cobalt Oxide Thermoelectric Compositions and uses thereof. US 20070039641 A1, 2007.

(15) Bevington, P.; Robinson, D. K. *Data Reduction and Error Analysis for the Physical Sciences*, 3rd ed.; McGraw-Hill: New York, NY, 2002.

(16) Balageas, D. L. Thermal diffusivity measurement by pulsed methods. *High Temp.-High Press* **1989**, *21*, 85−96.

(17) Pech-May, N. W.; Mendioroz, A.; Salazar, A. Generalizing the Flash Technique in the Front-Face Configuration to Measure the Thermal Diffusivity of Semitransparent Solids. *Rev. Sci. Instrum.* **2014**, *85*, 104902.

(18) Pech-May, N. W.; Vales-Pinzón, C.; Vega-Flick, A.; Cifuentes, Á.; Oleaga, A.; Salazar, A.; Alvarado-Gil, J. J. Study of the thermal properties of polyester composites loaded with oriented carbon nanofibers using the front-face flash method. *Polym. Test.* **2016**, *50*, 255−261.

(19) Maillet, D.; André, S.; Batsale, J. C.; Degiovanni, A.; Moyne, C. *Thermal Quadrupoles: Solving the Heat Equation through Integral Transforms*; Wiley: New York, NY, 2000.

(20) Abate, J.; Whitt, W. A Unified Framework for Numerically Inverting Laplace Transforms. *INFORMS J. Comput.* **2006**, *18*, 408−421.

(21) Forero-Sandoval, I. Y.; Pech-May, N. W.; Alvarado-Gil, J. J. Measurement of the Thermal Transport Properties of Liquids Using the Front-Face Flash Method. *Infrared Phys. Technol.* **2018**, *93*, 9−15.

(22) Shannon, R. D. Revised effective ionic radii and systematic studies of interatomic distances in halides and chalcogenides. *Acta Cryst. A* **1976**, *32*, 751−767.

(23) Harrington, R.; Miles, G. C.; West, A. R. Crystal chemistry of Co-doped Zn7Sb2O12. *J. Solid State Chem.* **2008**, *181*, 334−339.

(24) Iida, Y. Evaporation of Lithium Oxide from Solid Solution of Lithium Oxide in Nickel Oxide. *J. Am. Ceram. Soc.* **1960**, *43*, 171−172.

(25) Weidenfeld, G.; Weiss, Y.; Kalman, H. A Theoretical Model for Effective Thermal Conductivity (ETC) of Particulate Beds under Compression. *Granul. Matter* **2004**, *6*, 121−129.

(26) Naceur, H.; Megriche, A.; El Maaoui, M. Effect of Sintering Temperature on Microstructure and Electrical Properties of Sr1-x(Na0.5Bi0.5)xBi2Nb2O9 Solid Solutions. *J. Adv. Ceram.* **2014**, *3*, 17−30.

(27) Çengel, Y. A. *Heat Transfer: A Practical Approach*, 2nd ed.; McGraw-Hill: Boston, MA, 2002.

(28) Abeles, B. Lattice Thermal Conductivity of Disordered Semiconductor Alloys at High Temperatures. *Phys. Rev.* **1963**, *131*, 1906−1911.

(29) Tan, G.; Shi, F.; Sun, H.; Zhao, L.-D.; Uher, C.; Dravid, V. P.; Kanatzidis, M. G. SnTe-AgBiTe$_2$ as an efficient thermoelectric material with low thermal conductivity. *J. Mater. Chem. A* **2014**, *2*, 20849−20854.